Rapid Communications

Partially coherent axiconic surface plasmon polariton fields

Yahong Chen,[1,2,*] Andreas Norrman,[3] Sergey A. Ponomarenko,[4] and Ari T. Friberg[1]
[1]*Institute of Photonics, University of Eastern Finland, P.O. Box 111, FI-80101 Joensuu, Finland*
[2]*College of Physics, Optoelectronics and Energy, Soochow University, Suzhou 215006, China*
[3]*Max Planck Institute for the Science of Light, Staudtstraße 2, D-91058 Erlangen, Germany*
[4]*Department of Electrical and Computer Engineering, Dalhousie University, Halifax, Nova Scotia B3J 2X4, Canada*

(Received 24 October 2017; published 13 April 2018)

We introduce a class of structured polychromatic surface electromagnetic fields, reminiscent of conventional optical axicon fields, through a judicious superposition of partially correlated surface plasmon polaritons. We show that such partially coherent axiconic surface plasmon polariton fields are structurally stable and statistically highly versatile with regard to spectral density, polarization state, energy flow, and degree of coherence. These fields can be created by plasmon coherence engineering and may prove instrumental broadly in surface physics and in various nanophotonics applications.

DOI: 10.1103/PhysRevA.97.041801

Introduction. Electromagnetic surface waves have lately attracted ever-growing interest due to their unique physical properties and wealth of potential applications [1]. Surface plasmon polaritons (SPPs) [2], in particular, have given birth to the field of modern plasmonics [3], covering a rich diversity of multidisciplinary light physics [4–9]. Although plasmonics has mainly involved fully coherent electromagnetic fields to date, there has been increasing recognition that coherence can play an important role in controlling the spatial, spectral, and polarization distributions of SPPs [10–12]. A crucial step in this direction was taken recently by advancing a general theoretical framework to describe and customize the coherence of polychromatic SPPs in the Kretschmann setup [13]. Moreover, a simple and robust protocol to recover SPP field correlations from a far-field measurement was proposed [14]. Such plasmon coherence engineering can be instrumental for synthesizing structured SPP fields with desired spatiotemporal statistical properties.

In this Rapid Communication, we show how to design polychromatic structured SPP fields reminiscent of classic optical axicon fields [15,16] by superposing radially propagating SPPs of arbitrary correlations at a metal-air interface. We demonstrate that a whole class of such partially coherent surface fields—which we call axiconic surface plasmon polariton (ASPP) fields—with different intensities, polarizations, Poynting vectors, and degrees of coherence can be generated. We emphasize that, to our knowledge, all structured SPP fields studied so far have been either monochromatic (spatially and temporally coherent) [17–19] or polychromatic but spatially fully coherent [20,21]. In contrast, the ASPP fields are polychromatic and may have any degree of coherence. We also stress that we explore the coherence of SPP fields themselves rather than SPP-modified coherence of external fields. The partially coherent ASPP fields of high structural stability with respect to variations of the excitation circle radius and broad statistical versatility could find uses, e.g., in nanoparticle manipulation.

Field characterization. The field geometry, analogous to the traditional Kretschmann configuration [2], involves a homogeneous, isotropic, and nonmagnetic metal film deposited on a glass prism and located in the xy plane (see Fig. 1). The ASPP field at the planar metal-air surface ($z = 0$) is composed of uniformly distributed SPPs with origins along a circle centered at the point $\mathbf{r} = 0$ and of radius a. Such radially propagating SPPs can also be launched, for instance, with the help of radial gratings, plasmonic lenses, or optical metasurfaces [22–24]. We let $\mathbf{r}_0(\theta) = -a\hat{\mathbf{e}}_\parallel(\theta)$ represent the excitation point of an SPP that propagates in the direction of $\hat{\mathbf{e}}_\parallel(\theta) = \cos\theta\hat{\mathbf{e}}_x + \sin\theta\hat{\mathbf{e}}_y$ toward the circle center, where $0 \leqslant \theta < 2\pi$ is the azimuthal angle with respect to the x axis, whereas $\hat{\mathbf{e}}_x$ and $\hat{\mathbf{e}}_y$ are the Cartesian unit vectors in the x and y directions, respectively. Under these conditions, the spatial electric part of the ASPP field in air, for $(x^2 + y^2)^{1/2} \leqslant a$ and at (angular) frequency ω, can be written as [13]

$$\mathbf{E}(\mathbf{r},\omega) = \int_0^{2\pi} E(\theta,\omega)\hat{\mathbf{p}}(\theta,\omega)e^{i\mathbf{k}(\theta,\omega)\cdot[\mathbf{r}-\mathbf{r}_0(\theta)]}d\theta, \qquad (1)$$

where $E(\theta,\omega)$ is a complex-valued field amplitude of the monochromatic SPP at the excitation point, and

$$\mathbf{k}(\theta,\omega) = k_\parallel(\omega)\hat{\mathbf{e}}_\parallel(\theta) + k_z(\omega)\hat{\mathbf{e}}_z, \qquad (2)$$

$$\hat{\mathbf{p}}(\theta,\omega) = \hat{\mathbf{k}}(\theta,\omega) \times [\hat{\mathbf{e}}_z \times \hat{\mathbf{e}}_\parallel(\theta)] \qquad (3)$$

are the corresponding wave and unit polarization vectors, respectively. Furthermore, $\hat{\mathbf{k}}(\theta,\omega) = \mathbf{k}(\theta,\omega)/|\mathbf{k}(\omega)|$, with the wave-vector magnitude independent of θ, and $\hat{\mathbf{e}}_z$ is the Cartesian unit vector in the z direction. The film is thick enough (50–100 nm, Ag) so that mode overlap across the metal is negligible [25,26], whereby the tangential and normal wave-

*hon2019@163.com

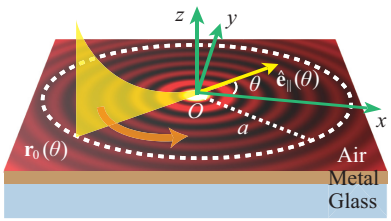

FIG. 1. Geometry and notations for the ASPP field synthesis. One of the contributing SPPs, excited on the circle of radius a at the metal-air interface and propagating in the direction of $\hat{\mathbf{e}}_\parallel(\theta)$, is explicitly displayed in the figure.

vector components in Eq. (2) read [2]

$$k_\parallel(\omega) = \frac{\omega}{c}\sqrt{\frac{\epsilon_r(\omega)}{\epsilon_r(\omega)+1}}, \qquad k_z(\omega) = \frac{\omega}{c}\sqrt{\frac{1}{\epsilon_r(\omega)+1}}, \tag{4}$$

where $\epsilon_r(\omega)$ is the (complex-valued) relative permittivity of the metal, accounting for dispersion and absorption, and c is the speed of light.

Next, we take $\mathbf{E}(\mathbf{r},\omega)$ in Eq. (1) to represent a field realization, whereupon the spectral electric coherence matrix, characterizing all the second-order statistical properties of a (stationary) polychromatic ASPP field, can be written as $\mathbf{W}(\mathbf{r}_1,\mathbf{r}_2,\omega) = \langle \mathbf{E}^*(\mathbf{r}_1,\omega)\mathbf{E}^{\mathrm{T}}(\mathbf{r}_2,\omega)\rangle$ [27,28]. Here the asterisk, superscript T, and angle brackets denote complex conjugate, matrix transpose, and ensemble average, respectively. It follows from Eqs. (1)–(3) that

$$\mathbf{W}(\mathbf{r}_1,\mathbf{r}_2,\omega) = e^{-2k_\parallel''(\omega)a}\iint_0^{2\pi} W(\theta_1,\theta_2,\omega)\mathbf{K}(\theta_1,\theta_2,\omega) \times e^{i[\mathbf{k}(\theta_2,\omega)\cdot\mathbf{r}_2 - \mathbf{k}^*(\theta_1,\omega)\cdot\mathbf{r}_1]}d\theta_1 d\theta_2, \tag{5}$$

where the double prime denotes the imaginary part,

$$W(\theta_1,\theta_2,\omega) = \langle E^*(\theta_1,\omega)E(\theta_2,\omega)\rangle \tag{6}$$

is the angular SPP correlation function, and

$$\mathbf{K}(\theta_1,\theta_2,\omega) = \hat{\mathbf{p}}^*(\theta_1,\omega)\hat{\mathbf{p}}^{\mathrm{T}}(\theta_2,\omega) \tag{7}$$

is a 3×3 matrix specifying the spectral polarization of the ASPP field. Equations (5)–(7) represent general polychromatic, partially coherent ASPP fields with the vectorial properties of all individual SPPs fully accounted for. The circle radius a acts effectively merely as a scaling factor of $\mathbf{W}(\mathbf{r}_1,\mathbf{r}_2,\omega)$—and thereby of all derivative quantities—highlighting the structural stability of the ASPP fields. From a practical standpoint, the SPP propagation length $l_{\mathrm{SPP}}(\omega) = 1/k_\parallel''(\omega)$ serves as a natural maximum radius. The correlation function $W(\theta_1,\theta_2,\omega)$, governing the salient statistical properties of the ASPP fields (see below), can be designed at will via plasmon coherence engineering, underlining the broad versatility of the ASPP fields.

Spectral density. To gain insight into the spectral density $S(\mathbf{r},\omega)$ of the ASPP fields, obtained from Eq. (5) as

$$S(\mathbf{r},\omega) = \mathrm{tr}\,\mathbf{W}(\mathbf{r},\mathbf{r},\omega), \tag{8}$$

with tr denoting the matrix trace, we consider two examples. In the first case the SPPs are fully correlated, whereby the angular correlation function factors as $W(\theta_1,\theta_2,\omega) = E^*(\theta_1,\omega)E(\theta_2,\omega)$, with the amplitudes taken in phase. In the second example the SPPs are completely uncorrelated such that $W(\theta_1,\theta_2,\omega) = \delta(\theta_1-\theta_2)|E(\theta_1,\omega)|^2$, where $\delta(\theta_1-\theta_2)$ is the Dirac δ-function. Moreover, in both cases the SPPs are assumed to have equal initial intensities, i.e., $|E(\theta,\omega)|^2 = |E(\omega)|^2 = I_{\mathrm{SPP}}(\omega)$. For the correlated field, Eqs. (2), (3), and (5)–(8) yield

$$S(\mathbf{r},\omega) = \mathcal{S}(z,\omega)\frac{|J_0[k_\parallel(\omega)\rho]|^2 + \kappa^2(\omega)|J_1[k_\parallel(\omega)\rho]|^2}{1+\kappa^2(\omega)}, \tag{9}$$

where $J_0[k_\parallel(\omega)\rho]$ and $J_1[k_\parallel(\omega)\rho]$ are (complex-valued) Bessel functions of the first kind and of orders 0 and 1, respectively, $\rho = (x^2+y^2)^{1/2}$ is the radial distance from the circle center, $\kappa(\omega) = |k_z(\omega)|/|k_\parallel(\omega)|$, and

$$\mathcal{S}(z,\omega) = 4\pi^2 I_{\mathrm{SPP}}(\omega)e^{-2k_\parallel''(\omega)a}e^{-2k_z''(\omega)z}. \tag{10}$$

For the uncorrelated superposition, we instead obtain

$$S(\mathbf{r},\omega) = (2\pi)^{-1}\mathcal{S}(z,\omega)I_0[2k_\parallel''(\omega)\rho], \tag{11}$$

where $I_0[2k_\parallel''(\omega)\rho]$ is a (real-valued) modified Bessel function of the first kind of order 0.

The spectral densities, valid up to $\rho = a$, are seen to be radially symmetric in both scenarios. When $a \lesssim l_{\mathrm{SPP}}(\omega)$, the maximum $S_{\max}(\mathbf{r},\omega)$ for the correlated ASPP field at any given z is located at the circle center ($\rho = 0$), whereas for the uncorrelated case it is always found at the circle's edge ($\rho = a$). The left panel of Fig. 2 illustrates the spectral density for the correlated ASPP field in the xy plane for a typical Ag-air interface at the free-space wavelength of $\lambda = 632.8$ nm when $a = l_{\mathrm{SPP}}(\lambda)$. The profile displays clearly the characteristic oscillatory pattern of an axicon field, similar to that of a plasmonic lens [17], with a strong and highly confined peak at the circle center, induced by interference among the SPPs. We return to the right panel of Fig. 2 later in connection with the degree of coherence of an uncorrelated SPP superposition.

To elucidate the spectral variations, we demonstrate in Fig. 3 the radial behavior of $S(\mathbf{r},\omega)$ (left panel) and the a-dependent shape of $S_{\max}(\mathbf{r},\omega)$ (right panel) for the correlated ASPP field discussed above in the visible regime. The left panel reveals

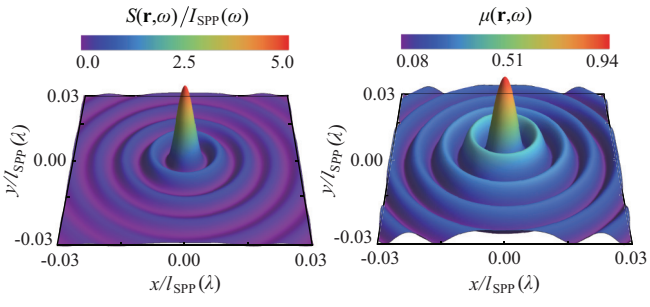

FIG. 2. (Left) Spectral density $S(\mathbf{r},\omega)$ for the correlated ASPP field and (right) the degree of coherence $\mu(\mathbf{r},\omega)$ for the uncorrelated ASPP field at an Ag-air interface for the free-space wavelength $\lambda = 632.8$ nm. In the left panel $I_{\mathrm{SPP}}(\omega)$ is the initial SPP intensity and $a = l_{\mathrm{SPP}}(\lambda)$, where a is the circle radius and $l_{\mathrm{SPP}}(\lambda)$ is the SPP propagation length. In the right panel $\mu(\mathbf{r},\omega)$ is independent of a, but $(x^2+y^2)^{1/2} \leqslant a$. The relative permittivity of Ag is from empirical data [29].

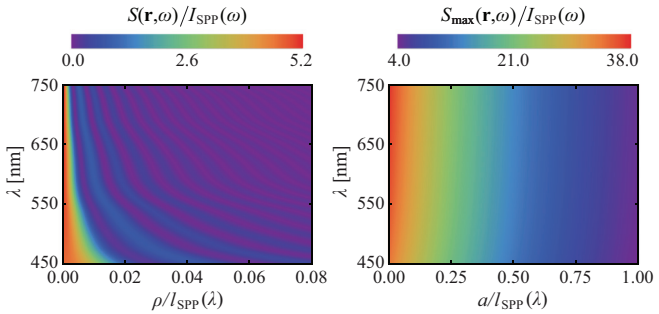

FIG. 3. (Left) Spectral density $S(\mathbf{r},\omega)$ for the correlated ASPP superposition as a function of the radial distance ρ and free-space wavelength λ for an Ag-air interface and circle radius of $a = l_{SPP}(\lambda)$, where $l_{SPP}(\lambda)$ is the SPP propagation length. (Right) Maximum of the spectral density $S_{max}(\mathbf{r},\omega)$ as a function of the circle radius a for the same field as in the left panel. Note that $S(\mathbf{r},\omega)$ and $S_{max}(\mathbf{r},\omega)$ are normalized with respect to the initial SPP intensity $I_{SPP}(\omega)$. Empirical data [29] are used for the relative permittivity of Ag.

that the peak confinement (and oscillation frequency) increases with respect to $l_{SPP}(\lambda)$ (depicted in the right panel of Fig. 4) as λ becomes larger; for red light the peak is localized inside a region as small as $\rho \approx l_{SPP}(\lambda)/500$, whereas for blue light it is constrained within $\rho \approx l_{SPP}(\lambda)/25$. The right panel indicates that $S_{max}(\mathbf{r},\omega)$ is practically independent of λ when $a/l_{SPP}(\lambda)$ is kept fixed and that it may even be tens of times greater than $I_{SPP}(\omega)$ when the circle radius is reduced.

We stress that the central spot is stable with respect to the circle radius (which only scales its magnitude) as long as the SPPs are correlated. When the SPP correlations become weaker, the spot gradually fades away and $S(\mathbf{r},\omega)$ gets smoothly distributed over the whole circle region. This is evidenced in the left panel of Fig. 4, displaying the ρ-dependent behavior of $S(\mathbf{r},\omega)$ for the uncorrelated ASPP field on an Ag-air boundary at $z = 0$ for selected values of a. The spectral density in Fig. 4 is effectively independent of the wavelength, and it exhibits smaller maxima (now at $\rho = a$) than in Fig. 3 since the SPPs do not interfere. The axicon-field-like pattern of Fig. 2

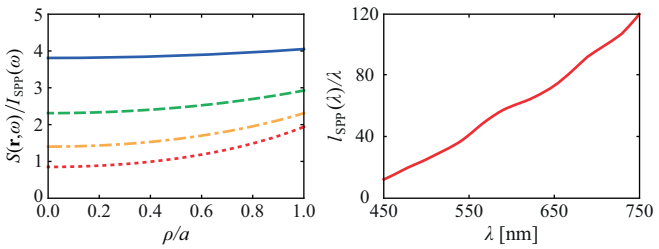

FIG. 4. (Left) Spectral density $S(\mathbf{r},\omega)$ for the uncorrelated ASPP field as a function of the radial distance ρ at an Ag-air interface when the circle radius a is varied: $a = 0.25\, l_{SPP}(\lambda)$ (the solid blue curve), $a = 0.50\, l_{SPP}(\lambda)$ (the dashed green curve), $a = 0.75\, l_{SPP}(\lambda)$ (the orange dashed-dotted curve), and $a = l_{SPP}(\lambda)$ (the red dotted curve). (Right) SPP propagation length $l_{SPP}(\lambda)$ as a function of the free-space wavelength λ for the Ag-air surface according to empirical data [29]. Note that the plots of $S(\mathbf{r},\omega)$ and $l_{SPP}(\lambda)$ are normalized with respect to the initial SPP intensity $I_{SPP}(\omega)$ and wavelength λ, respectively.

will remarkably reemerge in the degree of coherence for the uncorrelated SPP superposition field.

Polarization state. We examine the polarization state of the ASPP fields likewise in terms of the two examples. For correlated SPPs, the electric field, as obtained from Eq. (1), has at any point a radial component $E_\rho(\mathbf{r},\omega)$ and a transverse component $E_z(\mathbf{r},\omega)$ such that their ratio is

$$\frac{E_\rho(\mathbf{r},\omega)}{E_z(\mathbf{r},\omega)} = \frac{-ik_z(\omega)J_1[k_\parallel(\omega)\rho]}{k_\parallel(\omega)J_0[k_\parallel(\omega)\rho]}. \tag{12}$$

Several conclusions can be drawn from this result. Equation (12) is independent of z, but it is natural to consider it at the metal surface ($z = 0$). At the circle center the field is purely transverse, i.e., $E_\rho(0,\omega) = 0$, whereas for a large radius a the polarization state at the circle's edge ($\rho = a$) coincides with that of the corresponding individual SPP, i.e., $E_\rho(a,\omega)/E_z(a,\omega) = k_z(\omega)/k_\parallel(\omega)$. This is intuitive and follows from the asymptotic expressions of the Bessel functions. In between the center and the edge, the polarization state oscillates in the radial cross-sectional plane, determined by the Stokes parameters [28].

In the uncorrelated case, the polarization is specified by the 3×3 matrix $\mathbf{\Phi}(\mathbf{r},\omega) = \mathbf{W}(\mathbf{r},\mathbf{r},\omega)$, obtained from Eq. (5). It yields the position-independent ratio

$$\frac{\Phi_{xx}(\mathbf{r},\omega) + \Phi_{yy}(\mathbf{r},\omega)}{\Phi_{zz}(\mathbf{r},\omega)} = \kappa^2(\omega), \tag{13}$$

where $\kappa(\omega) = |k_z(\omega)|/|k_\parallel(\omega)|$ as before. For typical plasmonic metals (e.g., Ag and Au) we have $\kappa(\omega) \ll 1$ in the red part of the visible spectrum [29]. Hence at these frequencies, the uncorrelated ASPP field is highly polarized in the z direction. In the blue part of the spectrum, however, the field may acquire a significant parallel component (although the transverse component still is dominant). A rigorous vector-field treatment therefore is generally required. Considering only the parallel component, one finds that its degree of polarization [28] is given by $P(\mathbf{r},\omega) = I_2[2k''_\parallel(\omega)\rho]/I_0[2k''_\parallel(\omega)\rho]$, where $I_2[2k''_\parallel(\omega)\rho]$ is a modified Bessel function of the first kind of order 2. The parallel component is thus unpolarized at the center and turns monotonically to fully polarized at the circle's edge ($\rho = a$), provided a is large enough. By symmetry it is evident that the polarized part of the parallel field component points radially. These results, and those for the fully correlated case above, characterize the overall polarization behavior of the ASPP fields.

Energy flow. The energy flow of the ASPP fields can be assessed by taking the ensemble average of the (time-averaged) Poynting vector for harmonic fields [1], viz.,

$$\mathbf{S}(\mathbf{r},\omega) = \tfrac{1}{2}\langle \mathbf{E}(\mathbf{r},\omega) \times \mathbf{H}^*(\mathbf{r},\omega)\rangle', \tag{14}$$

where $\mathbf{H}(\mathbf{r},\omega)$ is a realization of the magnetic field and the prime stands for the real part. Like before, it is illustrative to examine the behavior of $\mathbf{S}(\mathbf{r},\omega)$ in terms of the correlated and uncorrelated ASPP fields. From Eqs. (1)–(3) and (14) we first obtain for the correlated superposition

$$\mathbf{S}(\mathbf{r},\omega) = \frac{1}{2Z_0}\frac{k_0(\omega)}{|\mathbf{k}(\omega)|^2}\mathcal{S}(z,\omega)(k'_z(\omega)|J_1[k_\parallel(\omega)\rho]|^2\hat{\mathbf{e}}_z - \{ik_\parallel(\omega)J_0[k_\parallel(\omega)\rho]J_1^*[k_\parallel(\omega)\rho]\}'\hat{\mathbf{e}}_\rho), \tag{15}$$

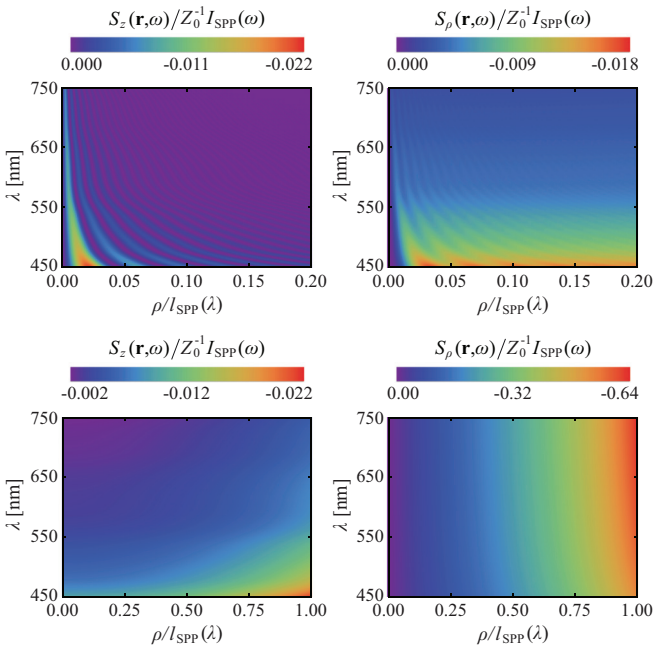

FIG. 5. (Left) Normal Poynting-vector components $S_z(\mathbf{r},\omega)$ and (right) radial Poynting-vector components $S_\rho(\mathbf{r},\omega)$ for the (top) correlated and (bottom) uncorrelated ASPP fields as a function of the radial distance ρ and free-space wavelength λ for an Ag-air surface and circle radius of $a = l_{\mathrm{SPP}}(\lambda)$, where $l_{\mathrm{SPP}}(\lambda)$ is the SPP propagation length. The relative permittivity of Ag is taken from empirical data [29]. Note that the Poynting-vector components are normalized with respect to the reciprocal free-space impedance Z_0^{-1} and the initial SPP intensity $I_{\mathrm{SPP}}(\omega)$.

whereas for the uncorrelated superposition we end up with

$$\mathbf{S}(\mathbf{r},\omega) = \frac{1}{4\pi Z_0}\frac{k_0(\omega)}{|\mathbf{k}(\omega)|^2}\mathcal{S}(z,\omega)\{k_z'(\omega)I_0[2k_\parallel''(\omega)\rho]\hat{\mathbf{e}}_z - k_\parallel'(\omega)I_1[2k_\parallel''(\omega)\rho]\hat{\mathbf{e}}_\rho\}. \tag{16}$$

Here Z_0 is the free-space impedance, $k_0(\omega) = \omega/c$ is the free-space wave number, $\mathcal{S}(z,\omega)$ is defined in Eq. (10), $\hat{\mathbf{e}}_\rho$ is the unit radial vector, and $\rho \leqslant a \lesssim l_{\mathrm{SPP}}(\omega)$.

As with the spectral densities, Eqs. (15) and (16) show that the Poynting vectors are radially symmetric and that their shapes are not affected by the circle radius a, again a reflection of the structural stability of the ASPP fields. In addition, the Poynting vector of the correlated ASPP field completely vanishes for $\rho = 0$, implying that no flow of energy occurs at the circle center. For the uncorrelated ASPP field, on the other hand, only the radial Poynting-vector component is zero at the origin, whereas the normal component is nonzero and negative since $k_z'(\omega) < 0$ [30]. This nonzero energy flow toward the surface is understood by realizing that the Poynting vector of the uncorrelated ASPP field is just a superposition of the Poynting vectors of the elementary SPPs, which always tilt toward the surface [30].

Figure 5 illustrates the spectral-radial behavior of the normal Poynting-vector components $S_z(\mathbf{r},\omega)$ and the radial Poynting-vector components $S_\rho(\mathbf{r},\omega)$ for the correlated and uncorrelated ASPP fields at an Ag-air surface when $z = 0$ and $a = l_{\mathrm{SPP}}(\lambda)$. The components of the correlated superposition (top panels) show oscillatory behaviors, similar to the spectral density in Fig. 3, with the amplitudes and periods increasing as the wavelength decreases. We also see that generally $S_z(\mathbf{r},\omega) < S_\rho(\mathbf{r},\omega)$. Nevertheless, there is a region very close to the circle center where the normal component of the correlated ASPP field dominates, in strong contrast with the energy-flow behavior of a single SPP [31]. Regarding $S_z(\mathbf{r},\omega)$ and $S_\rho(\mathbf{r},\omega)$ of the uncorrelated superposition (bottom panels), the oscillations are absent due to lack of SPP interference and $S_z(\mathbf{r},\omega) \ll S_\rho(\mathbf{r},\omega)$ inside the whole circle. Furthermore, the radial component of the uncorrelated ASPP field is spectrally nearly constant for a fixed $\rho/l_{\mathrm{SPP}}(\lambda)$. We note that the negativity of the Poynting-vector components in Fig. 5 signals that the energy flow is directed toward the surface and the circle center.

Degree of coherence. Excluding the scenario with fully correlated SPPs, in which case the ASPP field is coherent, the ASPP field exhibits partial coherence, specified by the SPP correlation function $W(\theta_1,\theta_2,\omega)$ in Eq. (6). To assess the spectral coherence properties of such a partially coherent ASPP field, vectorial in nature, we employ the electromagnetic degree of coherence [28,32],

$$\mu(\mathbf{r}_1,\mathbf{r}_2,\omega) = \frac{\|\mathbf{W}(\mathbf{r}_1,\mathbf{r}_2,\omega)\|_{\mathrm{F}}}{\sqrt{S(\mathbf{r}_1,\omega)S(\mathbf{r}_2,\omega)}}, \tag{17}$$

where $\|\cdots\|_{\mathrm{F}}$ refers to the Frobenius matrix norm. This real-valued quantity, bounded as $0 \leqslant \mu(\mathbf{r}_1,\mathbf{r}_2,\omega) \leqslant 1$, is a measure of the correlations existing between all the orthogonal components of the electric field at two points. The upper and lower limits correspond to full coherence and complete lack of coherence, respectively, whereas the intermediate values represent partial coherence.

As an example we examine the degree of coherence of the uncorrelated ASPP field, and for this we let $\mathbf{r}_1 = 0$. It follows from Eqs. (2), (3), (5)–(7), (10), (11), and (17) that under these conditions $\mu(\mathbf{r}_1,\mathbf{r}_2,\omega)$ depends only on the radial distance ρ of $\mathbf{r}_2 = \mathbf{r}$ from the circle center, i.e.,

$$\mu(\mathbf{r}_1,\mathbf{r}_2,\omega) = \mu(\mathbf{r},\omega) = \frac{1}{1+\kappa^2(\omega)}\left\{\frac{[2+\kappa^4(\omega)]|J_0[k_\parallel(\omega)\rho]|^2 + 4\kappa^2(\omega)|J_1[k_\parallel(\omega)\rho]|^2 + \kappa^4(\omega)|J_2[k_\parallel(\omega)\rho]|^2}{2I_0[2k_\parallel''(\omega)\rho]}\right\}^{1/2}, \tag{18}$$

where $J_2[k_\parallel(\omega)\rho]$ is a Bessel function of the first kind and order 2. Note that Eq. (18) is completely independent of the circle radius a but valid only up to $\rho = a \lesssim l_{\mathrm{SPP}}(\omega)$. In the right panel of Fig. 2 we illustrate $\mu(\mathbf{r},\omega)$ in the xy plane at an Ag-air boundary for $\lambda = 632.8$ nm, whereas Fig. 6 shows its spectral-radial structure. Both figures display distinct ringlike profiles characteristic of conventional axicon fields (cf., left panels in Figs. 2 and 3), but now for the degree

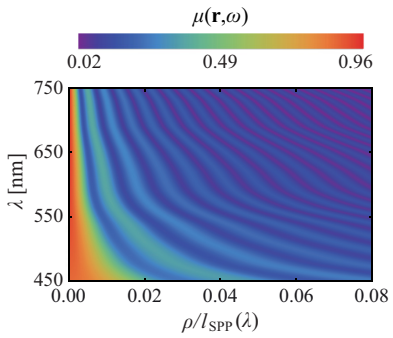

FIG. 6. Degree of coherence $\mu(\mathbf{r},\omega)$ of the uncorrelated ASPP field as a function of the radial distance ρ and free-space wavelength λ at an Ag-air surface. Empirical data [29] are used for the relative permittivity of Ag, and $l_{\mathrm{SPP}}(\lambda)$ is the SPP propagation length. Note the validity condition $\rho \leqslant a$ for $\mu(\mathbf{r},\omega)$, where a is the circle radius.

of coherence rather than the spectral density. We especially observe that $\mu(0,\omega) \approx 1$. This kind of behavior, which might appear counterintuitive as the SPPs are uncorrelated and thus do not interfere, originates from statistical similarity [33,34] of the SPPs at certain distances and is akin to the strong coherence modulation of two uncorrelated SPP modes [12–14]. Hence, for instance, the uncorrelated ASPP field is highly electromagnetically coherent near the center even when the circle radius is large [$a \sim l_{\mathrm{SPP}}(\lambda)$] and the SPPs are strongly attenuated [yet, as the SPP modes have different polarization states, $\mu(0,\omega) < 1$]. Allowing nonzero correlations among the SPPs and sculpting $W(\theta_1,\theta_2,\omega)$ by means of plasmon coherence engineering would enable one to synthesize the degree of coherence of the ASPP field into virtually any form.

Conclusions. We have introduced a class of polychromatic, partially coherent axicon-field-like surface electromagnetic fields via radially superposing SPPs of arbitrary correlations at a metal-air interface. Such generally vectorial ASPP fields were shown to possess high structural stability with respect to variations of the excitation circle radius and broad statistical versatility with regard to their spectral density, polarization state, flow of energy, and degree of coherence. For example, we demonstrated that fully correlated SPPs lead to a strong and highly confined spectral density peak at the center, whereas a totally uncorrelated SPP superposition exhibits a smoothly distributed intensity pattern. It was further shown that even an uncorrelated ASPP field displays an axicon-field-type pattern of partial coherence due to statistical similarity. In principle, the ASPP fields can be customized at will within the framework of plasmon coherence engineering, creating, for instance, fully or partially coherent SPP vortex fields or coherence lattice fields. Axiconic SPP fields may thus be especially useful for near-field interaction studies and nanoparticle manipulation applications.

Acknowledgments. This Rapid Communication was supported by the National Science and Engineering Research Council of Canada and the Academy of Finland (Project No. 310511). Y.C. thanks the China Scholarship Council (CSC), S.A.P. thanks the Joensuu University Foundation, and A.N. thanks the Swedish Cultural Foundation in Finland for financial support.

[1] J. A. Polo, Jr., T. G. Mackay, and A. Lakhtakia, *Electromagnetic Surface Waves* (Elsevier, Amsterdam, 2013).
[2] S. A. Maier, *Plasmonics: Fundamentals and Applications* (Springer, Berlin, 2007).
[3] A. A. Maradudin, J. R. Sambles, and W. L. Barnes, *Modern Plasmonics* (Elsevier, Amsterdam, 2014).
[4] A. Boltasseva and H. A. Atwater, Science **331**, 290 (2011).
[5] P. Berini and I. De Leon, Nat. Photonics **6**, 16 (2012).
[6] M. Kauranen and A. V. Zayats, Nat. Photonics **6**, 737 (2012).
[7] A. N. Grigorenko, M. Polini, and K. S. Novoselov, Nat. Photonics **6**, 749 (2012).
[8] M. S. Tame, K. R. McEnery, S. K. Özdemir, J. Lee, S. A. Maier, and M. S. Kim, Nat. Phys. **9**, 329 (2013).
[9] P. Genevet and F. Capasso, Rep. Prog. Phys. **78**, 024401 (2015).
[10] S. Aberra Guebrou, J. Laverdant, C. Symonds, S. Vignoli, and J. Bellessa, Opt. Lett. **37**, 2139 (2012).
[11] J. Laverdant, S. Aberra Guebrou, F. Bessueille, C. Symonds, and J. Bellessa, J. Opt. Soc. Am. A **31**, 1067 (2014).
[12] A. Norrman, T. Setälä, and A. T. Friberg, Opt. Express **23**, 20696 (2015).
[13] A. Norrman, S. A. Ponomarenko, and A. T. Friberg, EPL **116**, 64001 (2016).
[14] Y. Chen, A. Norrman, S. A. Ponomarenko, and A. T. Friberg, Opt. Lett. **42**, 3279 (2017).
[15] Z. Jaroszewicz, A. Burvall, and A. T. Friberg, Opt. Photonics News **16**, 34 (2005).
[16] Y. Wang, S. Yan, A. T. Friberg, D. Kuebel, and T. D. Visser, J. Opt. Soc. Am. A **34**, 1201 (2017).
[17] Z. Liu, J. M. Steele, W. Srituravanich, Y. Pikus, C. Sun, and X. Zhang, Nano Lett. **5**, 1726 (2005).
[18] A. Minovich, A. E. Klein, N. Janunts, T. Pertsch, D. N. Neshev, and Y. S. Kivshar, Phys. Rev. Lett. **107**, 116802 (2011).
[19] I. Dolev, I. Epstein, and A. Arie, Phys. Rev. Lett. **109**, 203903 (2012).
[20] D. M. Koller, A. Hohenau, H. Ditlbacher, N. Galler, F. Reil, F. R. Aussenegg, A. Leitner, E. J. W. List, and J. R. Krenn, Nat. Photonics **2**, 684 (2008).
[21] M. Ozaki, J.-I. Kato, and S. Kawata, Science **332**, 218 (2011).
[22] G. M. Lerman, A. Yanai, and U. Levy, Nano Lett. **9**, 2139 (2009).
[23] K. Y. Bliokh, Y. Gorodetski, V. Kleiner, and E. Hasman, Phys. Rev. Lett. **101**, 030404 (2008).
[24] J. Lin, J. P. Balthasar Mueller, Q. Wang, G. Yuan, N. Antoniou, X. Yuan, and F. Capasso, Science **340**, 331 (2013).
[25] A. Norrman, T. Setälä, and A. T. Friberg, Opt. Express **22**, 4628 (2014).
[26] A. Norrman, T. Setälä, and A. T. Friberg, Phys. Rev. A **90**, 053849 (2014).
[27] J. Tervo, T. Setälä, and A. T. Friberg, J. Opt. Soc. Am. A **21**, 2205 (2004).

[28] A. T. Friberg and T. Setälä, J. Opt. Soc. Am. A **33**, 2431 (2016).
[29] *Handbook of Optical Constants of Solids*, edited by E. D. Palik (Academic, Orlando, FL, 1998).
[30] A. Norrman, T. Setälä, and A. T. Friberg, Opt. Lett. **38**, 1119 (2013).
[31] K. Y. Bliokh and F. Nori, Phys. Rev. A **85**, 061801(R) (2012).
[32] J. Tervo, T. Setälä, and A. T. Friberg, Opt. Express **11**, 1137 (2003).
[33] S. A. Ponomarenko, H. Roychowdhury, and E. Wolf, Phys. Lett. A **345**, 10 (2005).
[34] T. Voipio, T. Setälä, and A. T. Friberg, J. Opt. Soc. Am. A **32**, 741 (2015).